Journal of Biomedical Optics

BiomedicalOptics.SPIEDigitalLibrary.org

# Photoacoustic lymphatic imaging with high spatial-temporal resolution

Catherine Martel
Junjie Yao
Chih-Hsien Huang
Jun Zou
Gwendalyn J. Randolph
Lihong V. Wang

SPIE.

Journal of Biomedical Optics 19(11), 116009 (November 2014)

# Photoacoustic lymphatic imaging with high spatial-temporal resolution

**Catherine Martel,[a,b,*,†] Junjie Yao,[c,†] Chih-Hsien Huang,[d] Jun Zou,[d] Gwendalyn J. Randolph,[a,*] and Lihong V. Wang[c,*]**

[a]Washington University School of Medicine, Department of Pathology and Immunology, 425 S Euclid, St. Louis, Missouri 63110, United States
[b]Université de Montréal, Faculty of Medicine; Montreal Heart Institute, 5000 Belanger Street, Montreal, Quebec H1T 1C8, Canada
[c]Washington University in St. Louis, Department of Biomedical Engineering, 1 Brookings Drive, St. Louis, Missouri 63130, United States
[d]Texas A&M University, Department of Electrical and Computer Engineering, College Station, Texas 77843-3128, United States

**Abstract.** Despite its critical function in coordinating the egress of inflammatory and immune cells out of tissues and maintaining fluid balance, the causative role of lymphatic network dysfunction in pathological settings is still understudied. Engineered-animal models and better noninvasive high spatial-temporal resolution imaging techniques in both preclinical and clinical studies will help to improve our understanding of different lymphatic-related pathologic disorders. Our aim was to take advantage of our newly optimized noninvasive wide-field fast-scanning photoacoustic (PA) microcopy system to coordinately image the lymphatic vasculature and its flow dynamics, while maintaining high resolution and detection sensitivity. Here, by combining the optical-resolution PA microscopy with a fast-scanning water-immersible microelectromechanical system scanning mirror, we have imaged the lymph dynamics over a large field-of-view, with high spatial resolution and advanced detection sensitivity. Depending on the application, lymphatic vessels (LV) were spectrally or temporally differentiated from blood vessels. Validation experiments were performed on phantoms and *in vivo* to identify the LV. Lymphatic flow dynamics in nonpathological and pathological conditions were also visualized. These results indicate that our newly developed PA microscopy is a promising tool for lymphatic-related biological research.  [DOI: 10.1117/1.JBO.19.11.116009]

Keywords: photoacoustic microscopy; high-speed imaging; lymphatic vessel; lymphatic dynamics.

Paper 140140RR received Mar. 4, 2014; revised manuscript received Sep. 2, 2014; accepted for publication Oct. 14, 2014; published online Nov. 19, 2014.

## 1 Introduction

First named the hepatico-aqueous vessels by Olaus Rudbeck in the 17th century,[1] the lymphatic vessels (LV) are part of a system that also comprises primary and secondary lymphoid organs. They consist of a one-way transport system that is essential for the transport of immune cells, absorption of dietary fats, and maintenance of normal fluid balance.[2–6] The blood and lymphatic vascular systems are two separate circulatory networks running in conjunction, having distinct but interdependent functions. They are first distinguishable by the way they transport their respective circulating fluids: the blood vasculature is a closed, high-pressure vascular system, whereas the lymph is transported in the tissues in an open, low-pressure vascular system.[7] In contrast to the blood vessels, lymphatic capillaries are blind-ending vessels characterized by elegantly organized junctions that are designed to absorb fluid, macromolecules, and cells from the parenchyma tissues of most organs. Once absorbed, these elements travel through the lymph that is pumped through the afferent collecting LV formed by pumping units called lymphangions. By generating contractions, the lymphangions are moving the lymph against adverse pressure gradient from the interstitium, creating a pressure to propel fluid from one lymphangion to the other.[8–12] Along with other factors such as the movement generated during respiration, muscle contractions, pulsations in the blood circulation and lymph formation *per se*,[13,14] they are essential in propelling the lymph to lymph nodes, the efferent collecting LV, the lymphatic ducts and ultimately to the blood circulation through one of the two subclavian veins.[7]

Because they are found in nearly all vascularized tissues, with the exception of bone marrow and the central nervous system other than the cerebrospinal fluid,[15] LV are integral to many physiological contexts. Lymphatic transport impairment and dysfunction are consequently associated with diverse severe pathologies. In addition to congenital or acquired lymphedema that are mostly characterized by swelling of the extremities and susceptibility to infections, malfunction of the lymphatic vasculature can lead to obesity, inflammation, and hypertension. In the last half decade, as we better understand the underlying genes that are responsible for the developmental and postnatal lymphatic growth, a substantial number of animal models have become available to evaluate the causes and consequences of lymphatic dysfunction.[16] Despite the fact that those newly developed mice greatly contribute to unraveling the role of the lymphatic system in different physiopathologic settings, techniques to image and quantify lymphatic vasculature in animal models and human patients still deserve attention. Improvement in imaging techniques would potentially push the limits of research on the roles and functions of the lymphatic network in physiologic and pathophysiologic contexts.

So far, several techniques aiming at offering real-time imaging and quantification of cell trafficking in LV or dynamic

*Address all correspondence to: Catherine Martel, E-mail: catherine.martel@icm-mhi.org; Gwendalyn J. Randolph, E-mail: grandolph@path.wustl.edu; Lihong V. Wang, E-mail: lhwang@wustl.edu

†These authors contributed equally to this work.

1083-3668/2014/$25.00 

visualization of the lymphatics *per se* have been used in intravital animal studies.[17–20] More recently, noninvasive and direct lymphatic imaging have been used in clinical trials: x-ray, computed tomography, magnetic resonance imaging (MRI), ultrasound, lymphoscintigraphy, and optical imaging have been broadly used to improve our understanding of different lymphatic-related pathologic disorders and to better understand the functional roles of the lymphatic vascular branching.[21–23] However, these often-high cost techniques do not allow the evaluation of the pulsing dynamics of the collecting vessels *per se*, mostly because of the poor spatio-temporal resolution they offer, or do not permit longitudinal imaging.

To the contrary, newly developed near-infrared (NIR) imaging methods, utilizing the NIR dye indocyanine green (ICG) as lymphatic tracers, are clinically approved and devoid of ionizing radiation, and allow the assessment of both the morphology of LV and lymphatic functions.[24–26] Despite their efficiency in permitting longitudinal imaging, ICG tracers are not optimal: it has been suggested that the injection of this dim dye that tends to aggregate in solution is related to inhibition of lymphatic contractions.[27] Recently, Proulx et al.[28] have identified a new macromolecular contrast agent for lymphatic imaging, and revealed in an experimental setting that the growth of metastases can lead to lymphatic flow obstructions in the primary draining lymph node. In their work, Proulx et al. utilized poly(ethylene glycol) conjugates of the bright NIR dye IRDye, and developed an NIR stereomicroscope for noninvasive visualization and quantification of the pulse rates and valvular function of collecting LV in mice. Because of the strong need for quantifying the overall pumping function, recent work by Nelson et al.[29] described a sophisticated pressure cuff system for quantifying the pumping capacity of collecting LV in the rat tail and forelimb using MRI integrated with a feedback-controlled pressure cuff to modulate lymph flow. Photoacoustic (PA) tomography, where the optical absorption contrast is acoustically detected, has also been actively used for mapping sentinel lymph nodes using various organic dyes or nanoparticles as the contrast agents.[30] However, these methods cannot provide depth information of the lymphatics. Since the lymphatic network located at different depths throughout the body can carry different characteristics and functional states, we believe that a three-dimensional (3-D) imaging tool with a large scanning range, high imaging speed, and uniform detection sensitivity is essential to better quantify the lymphatic function.

Herein, we take advantage of our newly developed fast-scanning optical-resolution PA microscopy (OR-PAM) to image the lymphatic network with high temporal-spatial resolution. By combining the OR-PAM with a fast-scanning water-immersible microelectromechanical system (MEMS) scanning mirror, we can finally image the lymph dynamic over a large field-of-view, while maintaining high resolution and detection sensitivity. Our approach may open a new window for a better understanding of different lymphatic dysfunction-related diseases and their relationship with inflammation, autoimmunity, and cancer.

## 2 Methods

### 2.1 *Experimental Mice*

Female ND4 Swiss Webster mice were purchased from Harlan Laboratory. CHY mouse embryos were purchased from the Medical Research Council (MRC Harwell, UK) on a mixed C3H/HeH and 101/H background. A colony was established in our animal facility at Washington University School of Medicine in St. Louis. Since one mutant allele is sufficient to confer loss of skin lymphatics,[31] all control mice were littermates bearing no copies of the mutations (wild-type mice). Experiments were conducted in compliance with approval of the Animal Studies Committee at Washington University.

### 2.2 *Animal Preparation for Imaging*

During the experiments, the animals' temperature was kept at 37°C by a water-circulating heating pad. Mice were anesthetized by inhalation of isoflurane with a concentration of 1.0% to 2.0% and air flow rate of 0.8 l/ min, and taped to a lab-made animal holder, which was mounted to the OR-PAM system. The mouse ear and tail were carefully positioned and fixed in place, thus limiting the potential motion artifacts that could be caused by the breathing during image acquisition. To image the lymphatic vasculature in the mouse ear or tail, intradermal injection of Evans blue (EB) dye (3% w/w) was carefully performed in the ear pinnae (10 $\mu$l) or the tail skin (50 $\mu$l), respectively, upstream of the imaged area, after the baseline images were acquired. Static areas of interest were imaged 10-min postinjection, whereas dynamic lymphatic flow was continuously imaged in a time span of 2 to 4 min.

### 2.3 *Imaging of the Lymphatic Vessels In Vivo*

The traditional OR-PAM[32] was used to image the LV *in vivo* [Fig. 1(a)]. Briefly, the nanosecond-pulsed laser beam from a dye laser (CBR-D, Sirah) pumped by an Nd:YLF laser (INNOSLAB, Edgewave) is tightly focused into the tissue surface by an optical objective (NA: 0.1 in air). The optical-acoustic beam combiner composed of a layer of silicone oil sandwiched by two prisms is used for the coaxial and confocal alignment of the optical illumination and acoustic detection. The resultant ultrasound waves are first focused by a concave acoustic lens (NA: 0.5 in water) ground into the bottom of the combiner, and then detected by a wideband ultrasonic transducer (V214-BB-RM, Olympus-NDT). A correction lens offsets the optical aberration of the prisms. Although each laser pulse generates a one-dimensional time-resolved signal, a 3-D image can be obtained by raster scanning the animal. The system has a lateral resolution of ca. 5 $\mu$m determined by the tight optical focusing, an axial resolution of ca. 15 $\mu$m determined by the transducer bandwidth, and a penetration depth of ca. 1 mm in highly scattering soft tissues. The cross-sectional imaging speed is ca. 1 Hz over a 3-mm scanning range.

To validate the two-wavelength identification of LV, the traditional OR-PAM was also used to image the blood- and EB-filled plastic tubes. Two tubes (diameter: 300 $\mu$m) were filled with oxygenated whole bovine blood and 0.3% EB solution, respectively, and imaged by OR-PAM in water at 560 and 595 nm with an excitation pulse energy of 100 nJ.

### 2.4 *Lymphatic Flow Dynamics*

Lymphatic flow dynamics were assessed with our recently developed wide-field fast-scanning OR-PAM with a water-immersible MEMS scanning mirror (MEMS-OR-PAM).[33] As shown in Fig. 1(b), a pulsed laser beam at 532 nm from a $Nd:YVO_4$ laser is focused by a condenser lens, then spatially

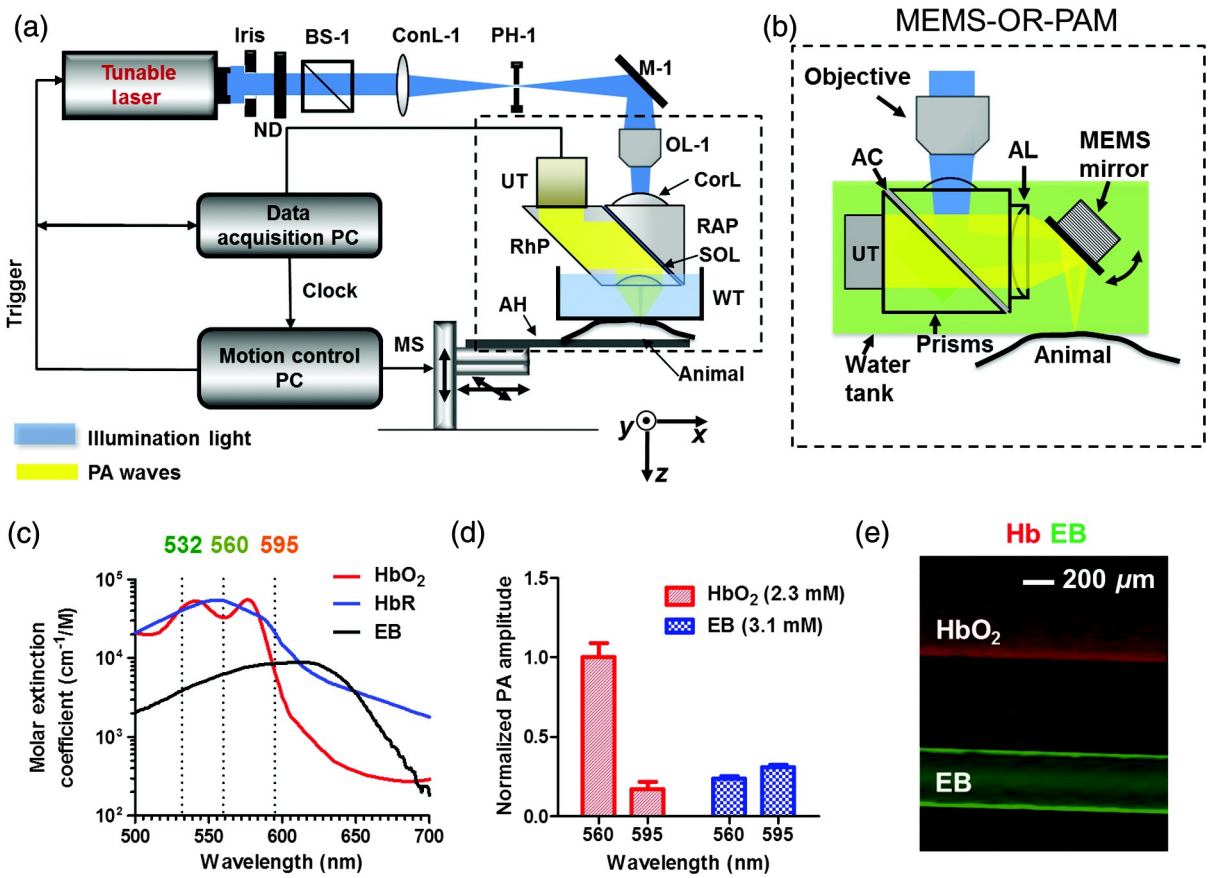


**Fig. 1** Optical-resolution PA microscopy (OR-PAM) systems. (a) Schematic of traditional OR-PAM system. AH, animal holder; BS, beam splitter; ConL, condenser lens; CorL, correction lens; M, mirror; MS, motorized stage; OL, objective lens; PH, pinhole; RAP, right angle prism; RhP, rhomboid prism; SOL, silicone oil layer; WT, water tank. (b) Schematic of fast-scanning MEMS-OR-PAM system. AC, aluminum coating; AL, acoustic lens. The MEMS-OR-PAM shares a similar light path outside the dashed box in (a). (c) Molar extinction spectra of oxy-hemoglobin ($HbO_2$), deoxy-hemoglobin (HbR), and Evans blue (EB). While 560 and 595 nm were used for two-wavelength measurement on traditional OR-PAM system, 532 nm was used for dynamic measurement on MEMS-OR-PAM. (d) The average PA signals of blood- and 0.3% EB-filled plastic tubes at 560 and 595 nm. (e) The identification of the blood-filled (shown in red) and EB-filled (shown in green) tubes by comparing the PA signals at two wavelengths.

filtered by a pinhole. The filtered laser beam is focused by an optical objective lens. A beam combiner provides acoustic-optical coaxial alignment. The focused laser beam and the generated PA waves are both directed by an MEMS scanning mirror plate. The PA waves are then focused by an acoustic lens and detected by an ultrasonic transducer. Driven by electromagnetic force, the whole MEMS scanning mirror can be submerged in water. Volumetric imaging is provided by fast angular scanning of the MEMS mirror along the $x$-axis and slow linear step-motor scanning of the sample along the $y$-axis. A 3-$\mu$m diffraction-limited lateral resolution and 26-$\mu$m axial resolution have been achieved, with a maximum penetration depth of 1.0 mm in soft tissue. The maximum in-focus scanning range is ~3.0 mm along the $x$-axis, with a cross-sectional frame rate of 400 Hz. By simultaneously scanning both the excitation laser beam and resultant acoustic beam, MEMS-OR-PAM maintains confocal alignment and thus high detection sensitivity over a large field-of-view.

### 2.5 *Statistics*

Data are expressed as the mean ± SD, unless otherwise indicated. Statistical differences were assessed using a two-tailed student's $t$-test. A $p$ value less than 0.05 is considered significant.

## 3 Results and Discussion

### 3.1 *Multiwavelength OR-PAM of Tube Phantoms*

Two plastic tubes were imaged by OR-PAM at 560 and 595 nm [Fig. 1(c)]. The $HbO_2$ concentration in the first tube was 2.3 mM, whereas the EB concentration in the other tube was 3.1 mM. The averaged PA signals' amplitudes from the two tubes at two wavelengths are shown in Fig. 1(d), after normalization to the PA signal of $HbO_2$ at 560 nm. The results show that the EB and $HbO_2$ have comparable PA signals at 595 nm. The difference of the PA signals at two-wavelengths was used to distinguish the two tubes [Fig. 1(e)]. Although the $HbO_2$ had a stronger PA signal at 560 nm than that at 595 nm (rendered in red), the EB had the opposite trend (rendered in green). The colors in Fig. 1(e) represent different absorbers, and the brightness represents the respective concentration. The averaged signal-to-noise ratio of EB at 595 nm is ~40 dB, suggesting a noise-equivalent detection sensitivity of ~31 $\mu$M.

### 3.2 *Multiwavelength OR-PAM of Lymphatic Vasculature at a Steady State*

EB injected intradermally was uptaken by lymphatic capillaries and provided the imaging contrast for OR-PAM. By using multi-wavelength measurements, we could spectrally separate the lymphatic vasculature from the blood vasculature *in vivo*. Before the injection of EB, the area of interest was imaged by OR-PAM at 595 nm, showing only the blood vessels [Fig. 2(a)]. Ten minutes after the injection, the same area of interest was imaged by the traditional OR-PAM at 560 and 595 nm [Fig. 2(b)]. Although hemoglobin in blood vessels has an absorption four times stronger at 560 nm than that at 595 nm, EB has an opposite absorption trend. Hence, blood vessels have a stronger signal amplitude at 560 nm, whereas LV filled with EB have a much stronger signal amplitude at 595 nm. Since blood vessels and LV are spatially separated, a direct comparison using a simple differential operation between the two images at 560 and 595 nm can be used to distinguish the LV from the blood vessels [Fig. 2(c)]. The colors in the figures represent different absorbers, and the brightness represents the respective concentration. The comparison of the PA images before and after the injection of EB further confirmed the identification of LV by using the two-wavelength method. In addition to the separation of the LV from blood vessels in a mouse ear, we also imaged the blood vessels and LV in a mouse tail [Figs. 2(d) and 2(f)]. The two forms of hemoglobin, deoxy-hemoglobin (HbR), and oxy-hemoglobin ($HbO_2$) can also be spectrally differentiated by the two-wavelength measurements, from which the oxygen saturation of hemoglobin ($sO_2$) can be computed [Fig. 2(e)].

### 3.3 *High-Speed MEMS-OR-PAM of Lymphatic Flow Dynamics*

We have then assessed the lymphatic flow dynamics by fast-scanning MEMS-OR-PAM. Although the mouse tail blood vasculature can be easily imaged [Figs. 3(a) and 3(b)], the visualization of the LV requires the intradermal injection of EB dye in the tip of the mouse tail. The dye is thus uptaken by lymphatic capillaries in the mouse tail and subsequently propelled into the collecting LV. Taking advantage of the volumetric imaging capability of MEMS-OR-PAM, we studied the lymphatic flow dynamics for both superficial LV (<300-$\mu$m deep) and deeper collecting LV (>1-mm deep). The region of interest was imaged with a volumetric frame rate of 2 Hz and a scanning step size of 5 $\mu$m, which was fast enough to assess the flow dynamics of the LV. In LV that were located closer to the epidermis, the overall signal intensity in the field-of-view was averaged to show the flow dynamics [Figs. 3(c) and 3(d), and 4]. In deeper LV, the temporal profile of the signal intensity was used to separate the LV from the blood vessels, since the blood vessel signal was maintained during the process [Figs. 3(e) and 3(f), and 5]. Furthermore, the lymph velocity and direction can be potentially quantified by comparing the

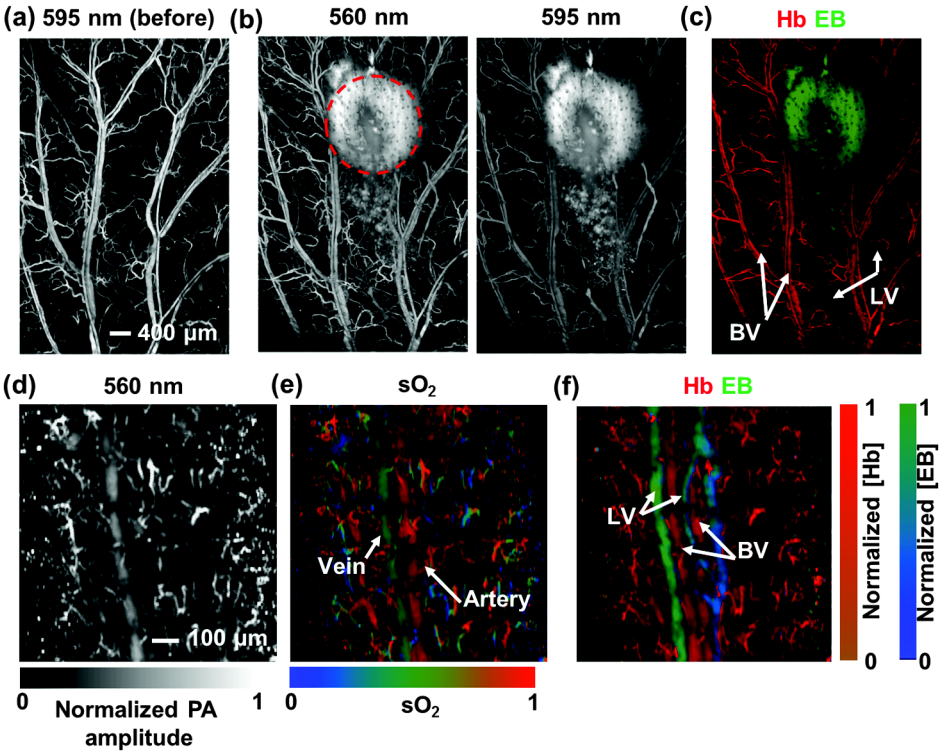


**Fig. 2** Traditional OR-PAM of LV in the skin of a mouse ear and tail. (a) PAM image of a mouse ear at 595 nm before the injection of EB, showing only blood vessels. (b) PAM images of the same mouse ear at 560 and 595 nm after the injection of 3% EB in the ear pinnae. (c) Spectral separation of the blood vessels (shown in red) and LV (shown in blue) in the ear skin. BV, blood vessels; LV, lymphatic vessels. (d) PAM image of a mouse tail vasculature at 560 nm before the EB injection. (e) PAM of the oxygen saturation of hemoglobin ($sO_2$) in the mouse tail, where the tail veins and arteries can be separated. (f) Spectral separation of blood vessels and LV in the tail after the EB injection.

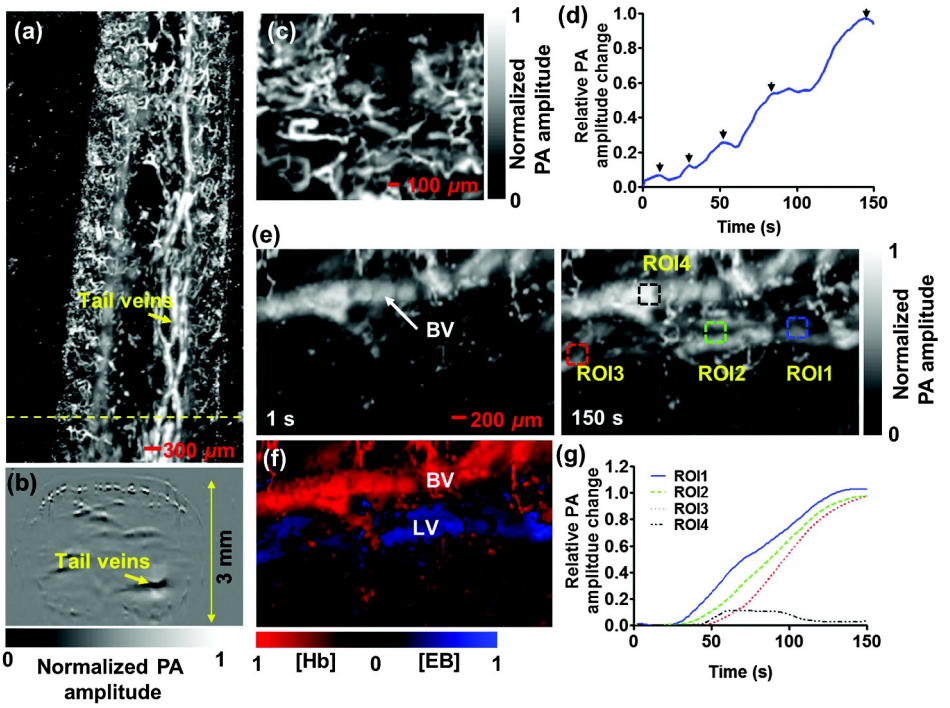


**Fig. 3** MEMS-OR-PAM of lymphatic flow dynamics in a mouse tail. (a) MEMS-OR-PAM of mouse tail blood vasculature. (b) A cross-sectional image of the mouse tail, showing the deep tail vein. (c) A snapshot of the dynamics of the superficial lymphatic capillaries in the mouse tail after the EB injection in the tail skin. (d) Time course of the relative PA amplitude change, where the arrows show the contractile rate of the lymphangions. (e) Snapshots of the dynamics of the collecting lymphatic vessel in a mouse tail after EB injection. (f) Blood vessels (shown in red) and collecting LV (shown in blue) were separated based on the temporal change in their signal strength. (g) Time courses of the relative PA signal changes at three regions of interest (ROI1-3) on the collecting lymphatic vessel and one region of interest (ROI4) on the blood vessel. The speed and direction of lymphatic flow can be extracted from time delays between ROI1 and ROI3.

temporal profiles of the PA signals from different regions along the LV [Fig. 3(g)].

We are aware that other physiological factors may affect the EB dye concentration during the flow measurement. For instance, the time window used for the temporal correlation will certainly affect the accuracy of the measurement. A longer time window measurement could potentially improve this accuracy, but the physiological conditions of the LV may change, as does the flow speed. Therefore, we view that an optimal time window should be chosen between the measurement accuracy and the temporal resolution of the measurement.

### 3.4 *High-Speed MEMS-OR-PAM of Mouse Model with Defected Lymphatic System*

In addition to the nonpathological conditions where the lymphatic system was intact (wild-type mice), we also studied the lymphatic dynamics of a genetically engineered mouse model that selectively lacks lymphatic capillaries in the skin.[31,34] This mouse mode has a point mutation in the tyrosine kinase domain of the VEGF-C receptor VEGFR3 that controls lymphatic vessel development.[35,36] Here, the so-called "CHY mice" were imaged by MEMS-OR-PAM and compared with wild-type

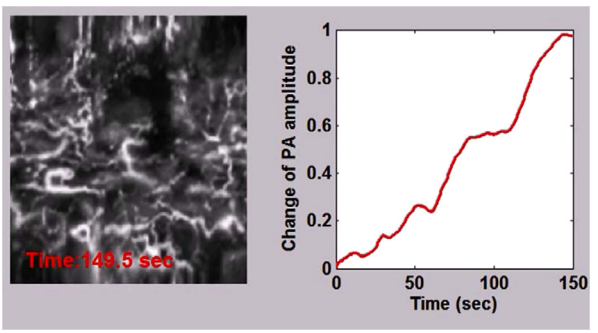


**Fig. 4** MEMS-OR-PAM of the superficial lymph flow dynamics in a mouse tail after Evans blue (EB) injection. The averaged PA signal amplitude is plotted on the right (MOV, 2.96 MB) [URL: http://dx.doi.org/10.1117/1.JBO.19.11.116009.1].

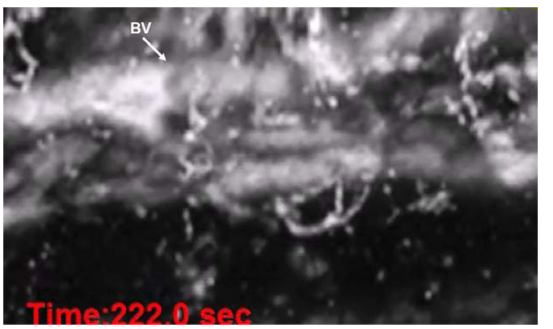


**Fig. 5** MEMS-OR-PAM of the flow dynamics in the collecting LV in a mouse tail. The EB was injected at the tip of the tail 50 s after the imaging started (MOV, 3.04 MB) [URL: http://dx.doi.org/10.1117/1.JBO.19.11.116009.2].

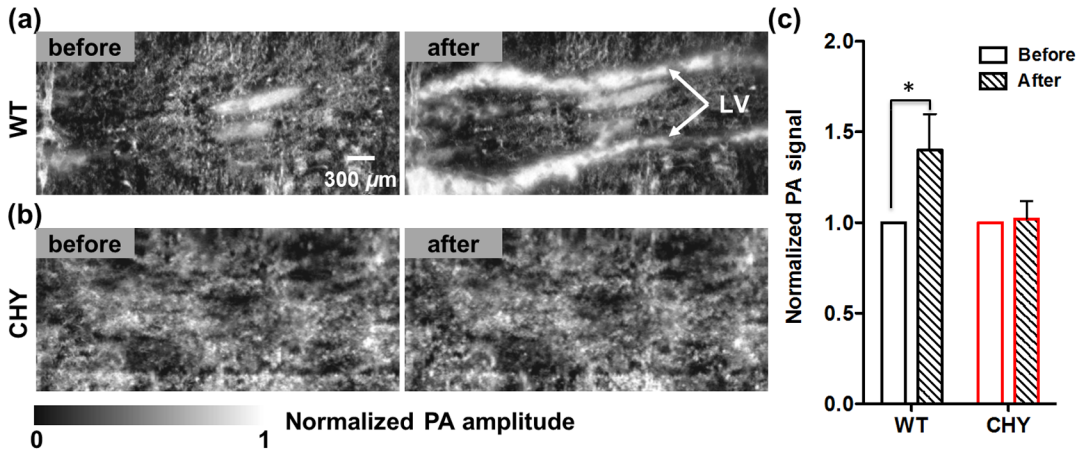


**Fig. 6** Lymphatic flow dynamics in nonpathological and pathological conditions. Snapshot MEMS-OR-PAM images of lymphatic flow dynamics of (a) wild-type and (b) CHY mice before and after EB injection. (c) Normalized PA signal. Bars: means ± SD. LV, lymphatic vessels. $*p \leq 0.05$.

littermate controls [Figs. 6(a) and 6(b)]. The region of interest, ~10-mm downstream from the injection site, was imaged with a volumetric frame rate of 2 Hz and a scanning step size of 5 $\mu$m, as shown in Figs. 7 and 8. The EB was injected 30 s after the imaging was started. Although we can clearly see the LV that quickly showed up after the EB injection in wild-type mice, we did not observe lymphatic flow in the CHY mice. For each mouse model, the signal intensity before and after the EB injection was quantified [Fig. 6(c)]. The results show that while the wild-type mice (Fig. 7) had a significant signal increase by 31% after the dye injection, the CHY mice (Fig. 8) did not show a noticeable signal increase, thus reflecting the lymphatic network defect in the skin of CHY mice.

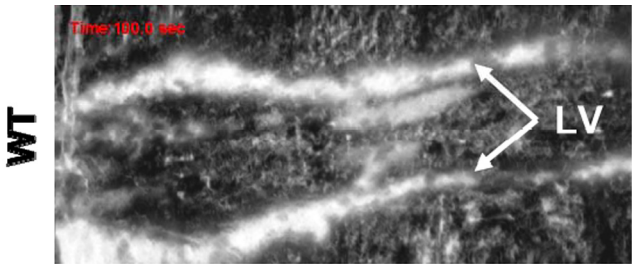


**Fig. 7** MEMS-OR-PAM of the lymph flow dynamics in a wild-type mouse tail. The EB was injected at the tip of the tail 30 s after the imaging started (MOV, 1.55 MB) [URL: http://dx.doi.org/10.1117/1.JBO.19.11.116009.3].

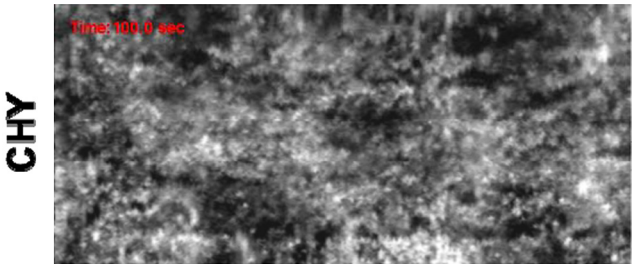


**Fig. 8** MEMS-OR-PAM of the lymph flow dynamics in a CHY mouse tail. The EB was injected at the tip of the tail 30 s after the imaging started (MOV, 2.40 MB) [URL: http://dx.doi.org/10.1117/1.JBO.19.11.116009.4].

## 4 Conclusions

Despite the implications in a wide range of diseases, such as lymphedema,[37] obesity,[38] diabetes,[39] asthma,[40] and atherosclerosis,[41] the understanding of the role of lymphatics in diseases is still limited. In the last decades, research unraveling the role of the lymphatic system in different physiopathologic settings has progressed exponentially primarily because of newly developed bioengineered mouse models and imaging techniques. However, when compared to the blood vasculature, the lymphatic network still represents distinctive challenges for noninvasive imaging in both animal models and humans, as well as for intraoperative visualization.

Herein, by using a novel imaging technique OR-PAM that combines a high speed, uniform detection sensitivity, and a large scanning range, we were able to image both the tissue lymphatic vasculature and lymph flow dynamics. Therefore, using high-speed OR-PAM could potentially provide both the structural and functional information for our understanding of the roles of lymphatics in diseases and promote the development of therapeutic interventions.

### *Acknowledgments*

We thank the manuscript editing and technical support from Prof. James Ballard, Dr. Chun-Cheng Chen, and Prof. William Chapman. This work was sponsored by NIH grants DP1 EB016986 (NIH Director's Pioneer Award), R01 CA186567 (NIH Director's Transformative Research Award), R01 CA134539, and R01 CA159959 (to L. V. Wang), R01 HL-096539 (to G.J. Randolph) and NSF grant CMMI-1131758 (to J. Zou). L. V. Wang has a financial interest in Endra, Inc., and Microphotoacoustics, Inc., which, however, did not support this work. Other authors have no conflicts of interest to declare.

### *References*

1. C. T. Ambrose, "Rudbeck's complaint: a 17th-century Latin letter relating to basic immunology," *Scand. J. Immunol.* **66**(4), 486–493 (2007).
2. R. M. Dongaonkar et al., "Balance point characterization of interstitial fluid volume regulation," *Am. J. Physiol. Regul., Integr. Comp. Physiol.* **297**(1), R6–R16 (2009).
3. J. Iqbal and M. M. Hussain, "Intestinal lipid absorption," *Am. J. Physiol. Endocrinol. Metab.* **296**(6), E1183–E1194 (2009).

4. J. R. Levick and C. C. Michel, "Microvascular fluid exchange and the revised Starling principle," *Cardiovasc. Res.* **87**(2), 198–210 (2010).
5. S. Liao et al., "Impaired lymphatic contraction associated with immunosuppression," *Proc. Natl. Acad. Sci. U. S. Am.* **108**(46), 18784–18789 (2011).
6. D. O. Miteva et al., "Transmural flow modulates cell and fluid transport functions of lymphatic endothelium," *Circ. Res.* **106**(5), 920–931 (2010).
7. T. Tammela and K. Alitalo, "Lymphangiogenesis: molecular mechanisms and future promise," *Cell* **140**(4), 460–476 (2010).
8. A. A. Gashev and D. C. Zawieja, "Hydrodynamic regulation of lymphatic transport and the impact of aging," *Pathophysiol.: Off. J. Int. Soc. Pathophysiol./ISP* **17**(4), 277–287 (2010).
9. D. C. Zawieja, "Contractile physiology of lymphatics," *Lymphatic Res. Biol.* **7**(2), 87–96 (2009).
10. M. Muthuchamy et al., "Molecular and functional analyses of the contractile apparatus in lymphatic muscle," *FASEB J* **17**(8), 920–922 (2003).
11. C. M. Quick et al., "Intrinsic pump-conduit behavior of lymphangions," *Am. J. Physiol. Regul., Integr. Comp. Physiol.* **292**(4), R1510–R15108 (2006).
12. P. Y. von der Weid and D. C. Zawieja, "Lymphatic smooth muscle: the motor unit of lymph drainage," *Int. J. Biochem. Cell Biol.* **36**(7), 1147–1153 (2004).
13. L. Causey, S. C. Cowin, and S. Weinbaum, "Quantitative model for predicting lymph formation and muscle compressibility in skeletal muscle during contraction and stretch," *Proc. Natl. Acad. Sci. U. S. A.* **109**(23), 9185–9190 (2012).
14. A. A. Gashev, "Lymphatic vessels: pressure- and flow-dependent regulatory reactions," *Ann. N. Y. Acad. Sci.* **1131**, 100–109 (2008).
15. M. Johnston et al., "Evidence of connections between cerebrospinal fluid and nasal lymphatic vessels in humans, non-human primates and other mammalian species," *Cerebrospinal Fluid Res.* **1**(1), 2 (2004).
16. G. Oliver and R. S. Srinivasan, "Lymphatic vasculature development: current concepts," *Ann. N. Y. Acad. Sci.* **1131**, 75–81 (2008).
17. R. M. Hoffman, "Imaging metastatic cell trafficking at the cellular level in vivo with fluorescent proteins," *Methods Mol. Biol.* **1070**, 171–179 (2014).
18. K. Hayashi et al., "Real-time imaging of tumor-cell shedding and trafficking in lymphatic channels," *Cancer Res.* **67**(17), 8223–8228 (2007).
19. E. I. Galanzha et al., "In vivo multispectral, multiparameter, photoacoustic lymph flow cytometry with natural cell focusing, label-free detection and multicolor nanoparticle probes," *Cytom. Part A: J. Int. Soc. Anal. Cytol.* **73**(10), 884–894 (2008).
20. E. I. Galanzha and V. P. Zharov, "Photoacoustic flow cytometry," *Methods* **57**(3), 280–296 (2012).
21. M. Moshiri et al., "Using lymphoscintigraphy to evaluate suspected lymphedema of the extremities," *AJR Am. J. Roentgenol.* **178**(2), 405–412 (2002).
22. F. Zhang et al., "Preclinical lymphatic imaging," *Mol. Imaging Biol.: MIB: Off. Publ. Acad. Mol. Imaging* **13**(4), 599–612 (2011).
23. V. Mumprecht et al., "In vivo imaging of inflammation- and tumor-induced lymph node lymphangiogenesis by immuno-positron emission tomography," *Cancer Res.* **70**(21), 8842–8851 (2010).
24. R. Sharma et al., "Quantitative imaging of lymph function," *Am. J. Physiol. Heart Circ. Physiol.* **292**(6), H3109–H3118 (2007).
25. M. Weiler, T. Kassis, and J. B. Dixon, "Sensitivity analysis of near-infrared functional lymphatic imaging," *J. Biomed. Opt.* **17**(6), 066019 (2012).
26. R. Sharma et al., "New horizons for imaging lymphatic function," *Ann. N. Y. Acad. Sci.* **1131**, 13–36 (2008).
27. A. A. Gashev, T. Nagai, and E. A. Bridenbaugh, "Indocyanine green and lymphatic imaging: current problems," *Lymphatic Res. Biol.* **8**(2), 127–130 (2010).
28. S. T. Proulx et al., "Use of a PEG-conjugated bright near-infrared dye for functional imaging of rerouting of tumor lymphatic drainage after sentinel lymph node metastasis," *Biomaterials* **34**(21), 5128–5137 (2013).
29. T. S. Nelson et al., "Minimally invasive method for determining the effective lymphatic pumping pressure in rats using near infrared imaging," *Am. J. Physiol. Regul., Integr. Comp. Physiol.* **306**(5), R281–R290 (2014).
30. T. N. Erpelding et al., "Sentinel lymph nodes in the rat: noninvasive photoacoustic and US imaging with a clinical US system," *Radiology* **256**(1), 102–110 (2010).
31. T. Makinen et al., "Inhibition of lymphangiogenesis with resulting lymphedema in transgenic mice expressing soluble VEGF receptor-3," *Nat. Med.* **7**(2), 199–205 (2001).
32. K. Maslov et al., "Optical-resolution photoacoustic microscopy for in vivo imaging of single capillaries," *Opt. Lett.* **33**(9), 929–931 (2008).
33. J. Yao et al., "Wide-field fast-scanning photoacoustic microscopy based on a water-immersible MEMS scanning mirror," *J. Biomed. Opt.* **17**(8), 080505 (2012).
34. A. M. Platt et al., "Normal dendritic cell mobilization to lymph nodes under conditions of severe lymphatic hypoplasia," *J. Immunol.* **190**(9), 4608–4620 (2013).
35. K. Alitalo, "The lymphatic vasculature in disease," *Nat. Med.* **17**(11), 1371–1380 (2011).
36. P. Saharinen et al., "Lymphatic vasculature: development, molecular regulation and role in tumor metastasis and inflammation," *Trends Immunol.* **25**(7), 387–395 (2004).
37. J. P. Sleeman and W. Thiele, "Tumor metastasis and the lymphatic vasculature," *Int. J. Cancer J. Int. Cancer* **125**(12), 2747–2756 (2009).
38. N. L. Harvey et al., "Lymphatic vascular defects promoted by Prox1 haploinsufficiency cause adult-onset obesity," *Nat. Genet.* **37**(10), 1072–1081 (2005).
39. P. Qu et al., "Study on pancreatic lymphatics in nonobese diabetic mouse with prevention of insulitis and diabetes by adjuvant immunotherapy," *Anat. Rec. Part A* **281**(2), 1326–1336 (2004).
40. M. Ebina, "Remodeling of airway walls in fatal asthmatics decreases lymphatic distribution; beyond thickening of airway smooth muscle layers," *Allergol. Int.: Off. J. Jpn. Soc. Allergol.* **57**(2), 165–174 (2008).
41. C. Martel et al., "Lymphatic vasculature mediates macrophage reverse cholesterol transport in mice," *J. Clin. Invest.* **123**(4), 1571–1579 (2013).



**Catherine Martel** is currently an assistant professor in the Department of Medicine at Université de Montréal/Research scientist at the Montreal Heart Institute, Montreal, Quebec, Canada.

**Junjie Yao** is currently a postdoctoral research associate in the Department of Biomedical Engineering at Washington University in St. Louis, Missouri.

**Chih-Hsien Huang** is currently a graduate student in the Department of Electrical and Computer Engineering at Texas A&M University, Texas.

**Jun Zou** is an associate professor in the Department of Electrical and Computer Engineering at Texas A&M University, Texas.

**Gwendalyn J. Randolph** is a professor in the Department of Pathology and Immunology at Washington University, in St. Louis, Missouri.

**Lihong V. Wang** holds the Beare distinguished professorship in the Department of Biomedical Engineering at Washington University, in St. Louis, Missouri.